Published in partnership with Nanjing Tech University



https://doi.org/10.1038/s41528-024-00350-y

Active-type piezoelectric smart textiles with antifouling performance for pathogenic control

Check for updates

Su Eon Lee^{1,10}, Hanna Lee ^{1,10}, Jang Hwan Kim^{3,10}, Jae Chul Park^{4,10}, Sooah Kyung⁵, Hayoung Choi², Su Hyun Baek², Jun Hyun Park¹, Sohyun Park⁵, Jeong-Min Kim⁶, Hye-Jun Jo⁶, Seung Hyeon Cho⁷, Jiwoong Kim⁵, Hojun Kim ^{4,8}, Seung Ho Han ⁹ ⋈, Jun Kyun Oh ² ⋈ & Bong Hoon Kim ¹ ⋈

Recently, an investigation into preventive measures for coronavirus disease 2019 (COVID-19) has garnered considerable attention. Consequently, strategies for the proactive prevention of viral pathogens have also attracted significant interest in the field of wearable devices and electronic textiles research, particularly due to their potential applications in personal protective equipment. In this study, we introduce smart textiles designed with optimized piezoelectric devices that exhibit antifouling performance against microorganisms and actively inactivate viruses. These active-type smart textiles, which incorporate advanced lead zirconate titanate (PZT) ceramics, a stretchable interconnector array, and polymeric fabric, demonstrate effective antifouling capabilities, detaching approximately 90% of *Escherichia coli* and 75% of SARS-CoV-2. Furthermore, they inactivate viruses, releasing ~26.8 ng of N protein from ruptured SARS-CoV-2, using ultrasonic waves within the wearable platform. Experimental results show that piezoelectric smart textiles significantly reduce the spread of COVID-19 by leveraging the electrical and acoustic properties of PZT ceramics.

The coronavirus disease 2019 (COVID-19) outbreak has posed a severe threat to humanity worldwide due to its rapid spread, the severity of its symptoms, and the challenges in treating the disease¹⁻⁴. This extraordinary situation has impacted public health, political conditions, and cultural norms, leading to significant changes in the human social system. Numerous scientists have focused on developing medical vaccines for severe acute respiratory syndrome coronavirus-2 (SARS-CoV-2)⁵⁻⁹. Although vaccines developed by companies (e.g., Moderna and Pfizer) have shown impressive results, they face challenges with new virus variants and issues in vaccine distribution and production. Therefore, supplementary measures are necessary to prevent the spread of COVID-19, including rapid and reliable diagnosis for fast isolation and contact tracing, and the elimination of transmission routes through the use of personal protective equipment (PPE) for COVID-19¹⁰⁻¹³.

In this context, wearable platforms have demonstrated significant potential in effectively preventing infectious diseases^{14–17}. They serve as a

frontline defense, protecting humanity from dangerous bacteria and viruses transmitted through airborne respiratory aerosols and droplets smaller than $100~\mu m^{18-22}$.

For example, wearable devices/nanomaterials designed to prevent COVID-19 have demonstrated outstanding results, including supersensitive biosensors based on reduced graphene oxide for sensing antibodies 10,23,24, automated wireless wearable devices for continuous biosignal monitoring to diagnose the disease swiftly and reliably 25-27, and a two-dimensional materials-based superhydrophobic mask for self-cleaning and aerosol filtration to prevent viral infection 28,29. However, these research findings, while powerful as adjuncts to vaccines, have a major limitation: their effectiveness largely depends on the surface properties of the nanomaterials (Supplementary Table 1). If the surfaces become contaminated, not only does their antifouling and antiviral performance decline rapidly and drastically 30-33, but complex sterilization processes are also required for

¹Department of Robotics and Mechatronics Engineering, DGIST, Daegu, 42988, Republic of Korea. ²Department of Polymer Science and Engineering, Dankook University, Yongin, 16890, Republic of Korea. ³Department of Materials Science and Engineering, Ajou University, Suwon, 16499, Republic of Korea. ⁴Center for Advanced Biomolecular Recognition, KIST, Seoul, 02792, Republic of Korea. ⁵Department of Materials Science and Engineering, Soongsil University, Seoul, 06978, Republic of Korea. ⁶Division of Emerging Infectious Diseases, KDCA, Cheongju, 28159, Republic of Korea. ⁷Safety Measurement Institute, Korea Research Institute of Standards and Science (KRISS), Daejeon, 34113, Republic of Korea. ⁸Division of Bio-Medical Science and Technology, KIST School, UST, 02792 Seoul, Republic of Korea. ⁹Electronic Convergence Materials & Devices Research Center, Korea Electronics Technology Institute (KETI), 13509 Seongnam, Republic of Korea. ¹⁰These authors contributed equally: Su Eon Lee, Hanna Lee, Jang Hwan Kim, Jae Chul Park. ⊠e-mail: shhan@keti.re.kr; junkyunoh@dankook.ac.kr; bonghoonkim@dgist.ac.kr

performance recovery. Furthermore, these approaches primarily focus on rapid diagnosis for isolation or tailored treatments for COVID-19 patients and cannot inactivate SARS-CoV-2 directly. Hence, innovative strategies capable of actively inactivating SARS-CoV-2 are required to prevent the spread of COVID-19.

To address these limitations, advancements in active-type prevention strategies, such as electronic devices, are required. These strategies offer antifouling performance against microorganisms and direct virus inactivation, providing continuous performance and functioning effectively under harsh conditions compared with passive-type strategies such as vaccines and surface treatments. In this study, we introduce piezoelectric smart textiles based on lead zirconate titanate (PZT), exploited as a functional material in flexible electronics (Supplementary Table 2), for an active type of PPE to prevent the transmission of bacteria and viruses. The acoustic-based antifouling program, which has primarily been applied to macro-scale systems, has been miniaturized to the level of a wearable device and applied to the fabrication of smart textiles. This is the first demonstration of smart textiles exhibiting active antifouling performance against various microorganisms using vibrations generated by ultrasonic waves. The textiles, with PZT-based ultrasonic transducers, a stretchable metal interconnector array, and a fabric matrix, demonstrate antifouling performance against bacteria (e.g., Escherichia coli (E. coli)) and viruses (e.g., SARS-CoV-2), even in droplets and high concentrations of bacterial and viral suspensions. Moreover, they can inactivate the viruses through the mechanical displacement that bursts the virus. We successfully confirmed the performance of the piezoelectric smart textile by integrating the ultrasonic transducer into a wearable platform, detecting N proteins from ruptured viruses, and identifying remaining viruses on the textile's surface. Notably, smart textiles maintain consistent high performance, even under harsh conditions, such as high concentrations of bacterial and viral suspensions. Thus, developing PZT-based smart textile platforms with antifouling and antiviral capabilities is expected to pave the way for new opportunities in the field of smart textiles and biomedical applications.

Results

Designs and principles for the active-type piezoelectric smart textiles

Figure 1a illustrates the operating principle and an exploded illustration of the PZT-based ultrasonic smart textile. Ultrasonic waves emitted from the PZT-based ultrasonic transducer enhance the antifouling performance against bacteria (*E. coli*) and viruses and actively inactivate the coronavirus. The ultrasonic transducers are arranged in a 2 × 2 array and connected by stretchable metal interconnectors, which consist of a bilayer of polyimide (PI; thickness of $\approx 3~\mu m$) and copper (Cu; thickness of $\approx 20~\mu m$), encapsulated with a silicone elastomer for insulation and a hydrophobic surface (see details in Method section and Supplementary Fig. 1). The entire assembly is integrated into a nylon textile, providing a robust barrier against moisture and protecting against the absorption of aerosols and droplets containing bacteria and viruses.

We used a piezoelectric ceramic composed of 0.65Pb(Zr_{0.465}Ti_{0.545})O₃-0.35 $Pb(Zn_{0.167}Ni_{0.167}Nb_{0.666})O_3$ (PZT-PZNN; thickness: \approx 420 μm). For high power density and effective power delivery to the functional smart textiles, silver (thickness: ≈10 µm) is used as conductive electrodes (Fig. 1b, left; see details in Method section). To confirm the microstructure and layers of the PZT composite, we examined the scanning electron microscopy (SEM) image of the ceramic (Fig. 1b, right) that reveals dense microstructures with consistent grain size (≈ 1 μm) and uniform layer thickness of the ceramic³⁴. Figure 1c displays the X-ray diffraction (XRD) pattern of the PZT-PZNN ceramic, indicating a well-formed homogeneous perovskite structure without secondary phases (see details in Method section). Figure 1d shows the polarization-electric field (P-E) hysteresis curve of the PZT ceramic, demonstrating its typical ferroelectric state and confirming the absence of any internal bias (see details in Method section). Figure 1e presents a photographic image of piezoelectric smart textiles with a 4×5 array of ultrasonic transducers. These textiles contain square-shaped and circular

piezoelectric ceramic islands (dimensions: 5 mm \times 5 mm and a diameter of 1 cm, respectively), connected by stretchable metal interconnects (see details in Supplementary Fig. 2). Figure 1f illustrates the working principle of the antifouling functional smart textiles. The ultrasonic transducers can generate a mechanical displacement of PZT islands up to \approx 3.5 nm, providing continuous antifouling performance and preventing the attachment of aerosols and droplets to their surfaces. Furthermore, these mechanical vibrations are transmitted to the PZT islands embedded in the nylon fabric, creating an antifouling effect across the entire smart textiles. The PZT-based ultrasonic smart textile offers economic feasibility (see details in Supplementary Note 1).

Mechanical, electrical, and ultrasonic properties of the PZTbased transducers

Figure 2a-c illustrates the mechanical properties of the bare PZT-based piezo-ultrasonic assembly, demonstrating its potential for application in smart textiles or wearable devices under tensile stress. After the arrays have fully been unraveled by stretching, the tensile strain in the Cu electrodes increases rapidly, defining the stretching limit of the arrays. Both simulations and experiments indicate that up to 30% biaxial stretching results in irreversible deformation of the arrays upon release³⁵ (see details in Supplementary Note 2). Figure 2a presents an optical microscopic (OM) image of a 2 × 2 array of elements that can be reversibly stretched up to 30% in the biaxial direction. Finite element analysis (FEA) results of the arrays and the integrated arrays with fabric (nylon; dimensions: 10 mm × 10 mm and thickness of ≈500 µm) substrates reveal calculated tensile strains (maximum ≈2%) produced by the biaxial stretching, as shown in Fig. 2b, c. These strains are substantially lower than the fracture and yield values of each integrated material³⁶. Considering that human skin exhibits a linear elastic response to a tensile strain of 20%, these experimental results suggest that the island bridge architecture materials are suitable for wearable device applications^{29,37,38}.

The ultrasonic transducer actively converts electrical potentials from the top and bottom electrodes into mechanical vibrations and vice versa, thereby enhancing both bursting and antifouling performance. To validate this strategy, we present the measured impedance and phase angle spectra of the square/circle-shaped ultrasonic transducer islands as shown in Fig. 2d, e. The black curves represent the impedance of the ultrasonic transducers across the frequency spectrum, indicating the resonance frequencies (f_r) of the square-shaped ultrasonic transducer (410 kHz) and the circular-shaped ultrasonic transducer (196 kHz), and the antiresonance frequencies (f_a) of the square-shaped ultrasonic transducer (410.5 kHz) and the circularshaped ultrasonic transducer (211.5 kHz). The red curves depict the phase angles of the ultrasonic transducers according to the frequency spectrum. To illustrate the changes in the resonance-antiresonance frequencies according to the geometric design of our transducers, 3D finite element parametric modeling was conducted in COMSOL Multiphysics, as shown in Supplementary Fig. 5. The resonance-antiresonance frequencies are similar in both simulation and experimental data. Quantitative differences between the simulations and the experimental results might be attributed to vibration damping from the use of flexible polyimide, Cu film electrodes, and adhesives (Supplementary Fig. 3). Figure 2f, g exhibit the results of the pulse-echo signal at its f_r in an air medium. These results confirm that ultrasonic transducers can transmit and receive pulses in the air and in droplets. Figure 2h, i depict the measured displacement results of ultrasonic transducers fabricated with square/circle-shaped islands according to their frequency spectrum. The curves display the maximum displacements of ≈0.2/1 nm (2 V; black curves), 0.3/1.5 nm (4 V; red curves), and 0.6/3.5 nm (8 V; blue curves) at the f_r . These vibration capabilities, specific to each shape, contribute to the antifouling performance (square-shaped ultrasonic transducer) and the rupturing performance (circle-shaped ultrasonic transducer), thereby enhancing the functionality of smart textiles. Additionally, we measured the electrical, mechanical, and ultrasonic properties of ultrasonic transducers of dimensions 15 mm × 15 mm to facilitate the use of ultrasonic transducers of other dimensions for various applications (see details in

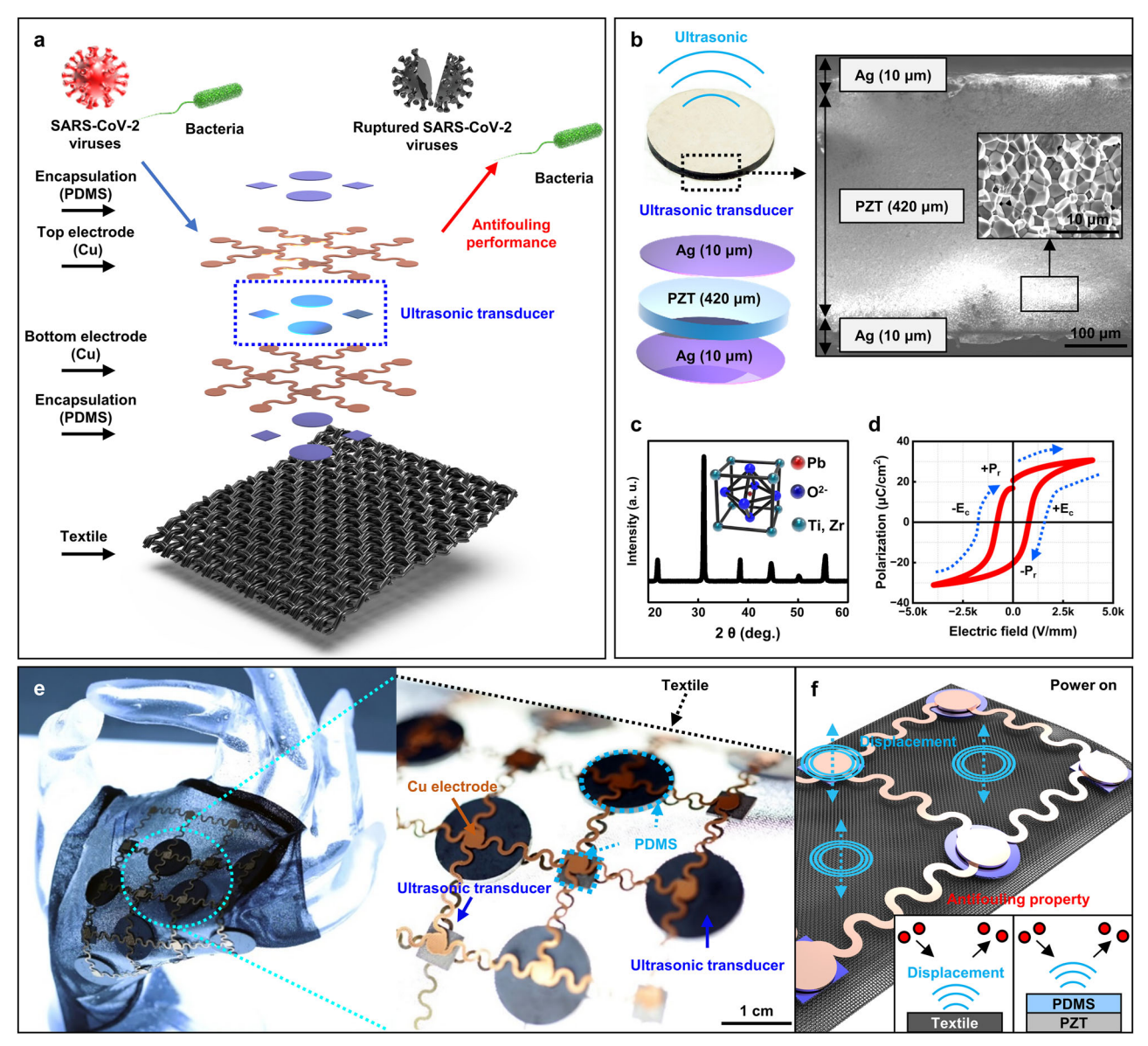


Fig. 1 | Design and functionality of the smart textile for antifouling performance and virus rupture. a Schematic of the smart textile illustrating its components, the ruptured virus, and the textile's antifouling performance. b Optical image and exploded schematic of the ultrasonic transducer (left), alongside a cross-sectional SEM image, showing the microstructures of the PZT (right). c XRD pattern of the

PZT ceramics and an illustration of the crystal structure. **d** P-E hysteresis curve of the poled PZT ceramics, demonstrating the ceramics' performance for piezoelectricity. **e** Photographic image of the textile bent around a hand-shaped form (left), and a detailed photographic image displaying the textile's scale and elements (right). **f** Illustration of the antifouling mechanism in the on-state smart textiles.

Supplementary Fig. 4–6). Also, reusability tests were also conducted on smart textiles composed of unit pixels of square and circular ultrasonic transducers, and are expected to have long-term durability (see details of the reusability test of ultrasonic transducer in the Method section).

Antifouling performances against cellular microorganisms

Based on the deep understanding of the ultrasonic properties of the bare PZT-based piezo-ultrasonic assembly, the anti-biofouling function of the PZT-based ultrasonic transducer integrated into smart textiles was demonstrated. Figure 3a presents a schematic of the antifouling performance of the PZT-based ultrasonic transducer integrated into smart textiles with PDMS against *E. coli* in both droplet (left) and suspension conditions (right). The ultrasounds emitted from the PZT-based ultrasonic transducers actively remove bacteria from the textile surface, resulting in a protective effect known as antifouling performance. Figure 3b displays an analysis of the smart textiles' performance using optical profilometry (top), OM

(middle), and photographic images (bottom). It also examines the properties of droplet size on the textile surface (right) under alternating off/on states. The results show that droplets (50–180 μm in height and 200–500 μm in diameter; black curves) are effectively displaced (red curves) due to the antifouling performance of the textiles. Figure 3c shows the SEM images of the textiles with sprayed bacterial droplets under off/on states. These images confirm that bacterial droplets are displaced by the ultrasonic waves, aligning with the results of the image analysis. When the ultrasonic transducer is turned off, the mean density of bacteria attached to the surface at the bacterial suspension condition is 7.4 log cells/mm² and at the bacterial droplet condition is 7.8 log cells/mm², respectively. When the ultrasonic transducer is turned on, the mean density of bacteria attached to the surface at the bacterial suspension condition decreases to 6.4 log cells/mm² and at the bacterial droplet condition to 6.8 log cells/mm². These results demonstrate a decrease in bacterial attachment by >1 log unit in the on state compared with the off state, indicating that the ultrasonic transducer

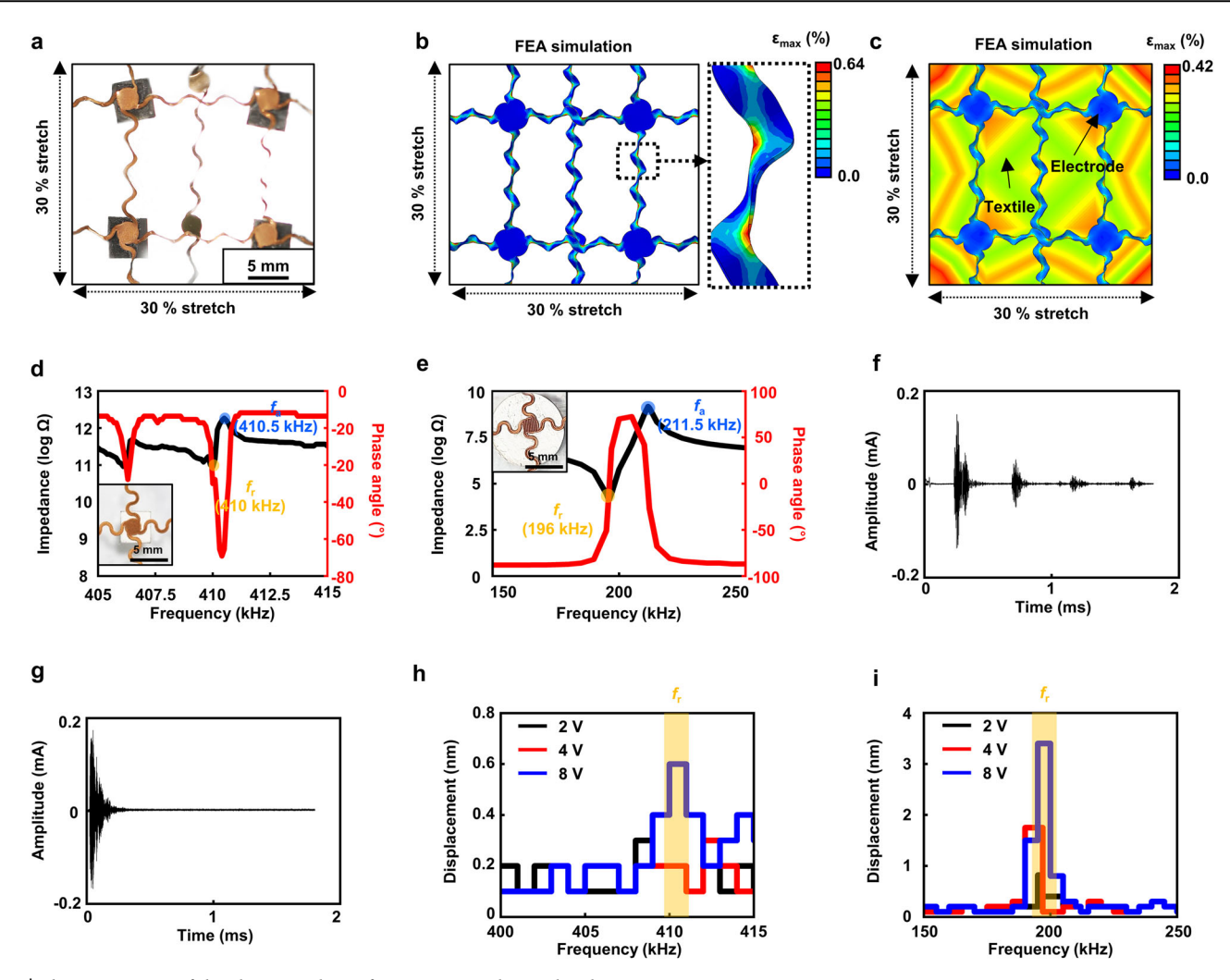


Fig. 2 | Characterization of the ultrasonic device focusing on its electrical and mechanical properties. a Experimental and simulation test results for 30% biaxial tensile stretching of the smart textiles. b Simulation results without the fabric. c Simulation results with the fabric incorporated. Impedance and phase angle spectra of the ultrasonic transducers fabricated with d a square-shaped PZT and e a circle-

shaped PZT, demonstrating piezoelectricity and the optical image. f Sent pulse signal and g received echo signal by the ultrasonic transducers through an air medium. Displacement of the ultrasonic transducers according to the frequencies and voltages integrated with h square-shaped PZT and (i) circle-shaped PZT.

improves the antifouling performance with both bacterial suspension and droplet conditions (Fig. 3d). Figure 3e displays the weight variation of the smart textiles in both off and on states, with sprayed droplets on their surface. Starting with sprayed droplets of 1 g at standard ambient temperature and pressure, the weight of the smart textiles decreases (\approx 0.15 g over 30 min and \approx 0.27 g over 60 min in the off state, \approx 0.28 g over 30 min, and \approx 0.47 g over 60 min in the on state). These results suggest that the observed weight loss is attributable not only to droplet evaporation but also to the functioning of the smart textiles. This confirms the antifouling performance of the smart textiles under droplet conditions.

Figure 3f presents the pour plating data, which varies with the voltages applied, alongside the SEM images of the surface from the bacteria experiments. The number of bacteria attached to the square-shaped ultrasonic transducers at 0 V, 4 V, and 8 V was $6.2\pm0.3\log$ CFU/mL, $5.0\pm0.2\log$ CFU/mL, and $4.7\pm0.2\log$ CFU/mL, respectively. These results indicate a reduction in bacterial attachment of over 1 log unit following ultrasonic transducer treatments, demonstrating the effectiveness of this method in enhancing antifouling performance. The SEM images corroborate that the ultrasonic transducer effectively prevents bacterial attachment to the surface. Figure 3g presents a graph depicting the number of bacteria attached to the surface of the ultrasonic transducers at 0 V (8.2 \pm 0.3 log CFU/mL) and compares it to those fabricated with square-shaped

 $(5.4\pm0.4\log$ CFU/mL) and circular-shaped $(5.3\pm0.5\log$ CFU/mL) ultrasonic transducers. Figure 3h shows the number of bacteria attached to the surface of the textile (Nylon; $7.3\pm1.3\log$ CFU/mL), the textile at 0 V $(9.7\pm1.2\log$ CFU/mL), and the smart textile at 8 V $(6.2\pm0.6\log$ CFU/mL). These results demonstrate a significant decrease in bacterial attachment by $\approx90\%$, thereby experimentally confirming the antifouling performance of the smart textile.

Notably, the impact of PDMS surface properties on the antifouling performance is expected to be minimal, as PDMS encapsulation is applied only to the electrodes, which are a small part of the integrated ultrasonic transducer. Furthermore, the active type smart textile is anticipated to maintain excellent antifouling properties compared with the hydrophobic surface, without concerns regarding surface contamination that causes performance degradation, which can occur with passive type antifouling strategies.

Antifouling and rupturing performances against non-cellular microorganisms

We investigate the antifouling and rupturing performance of an ultrasonic transducer integrated smart textile with PDMS against the coronavirus (SARS-CoV-2) using experiments with inactivated viruses. Figure 4a provides schematic illustrations and experimental data demonstrating the

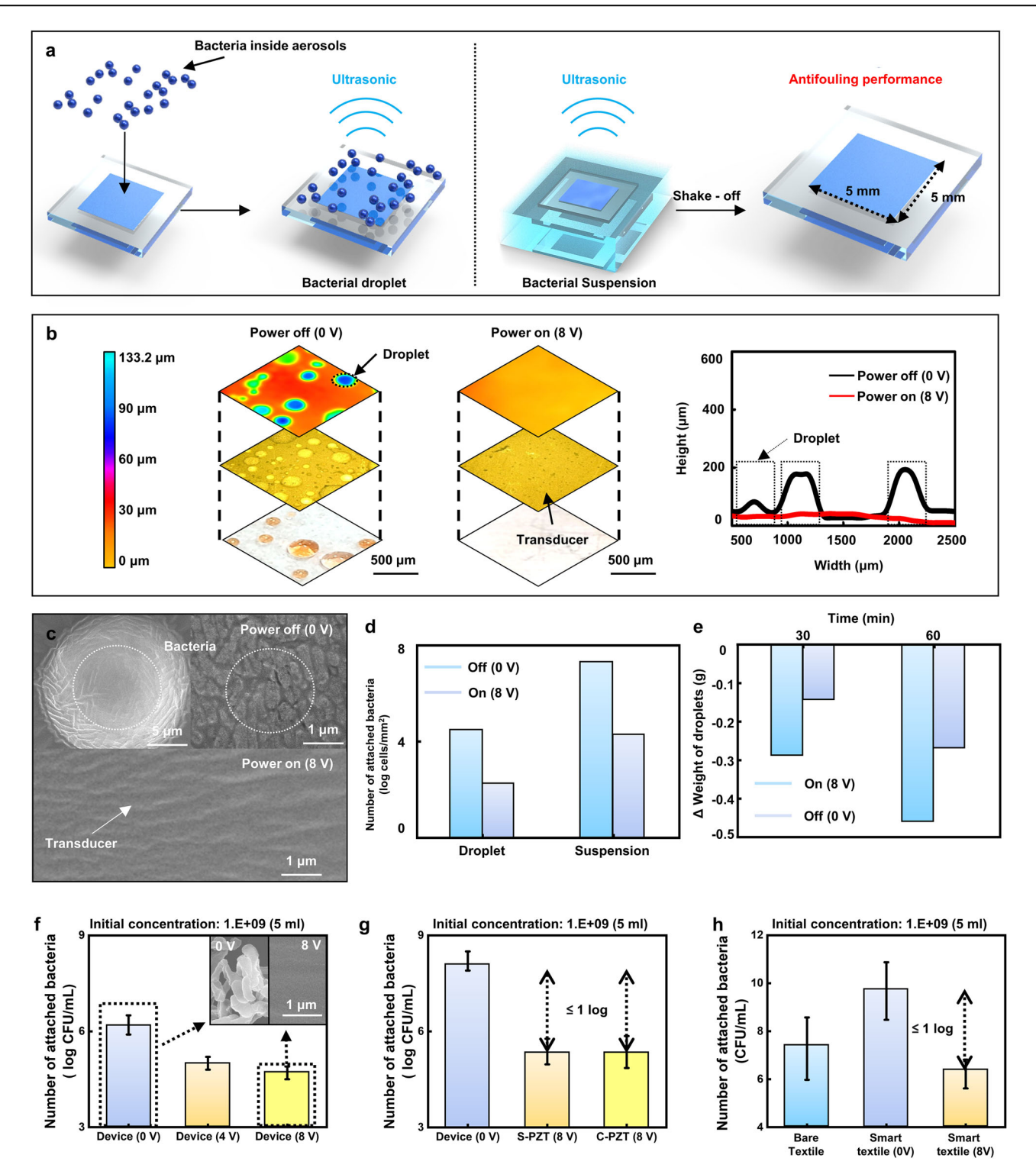


Fig. 3 | Experiments with bacteria (*E. coli*) and the evaluation of antifouling performance under various conditions. a Schematic illustrating the antifouling principles against bacterial droplets and suspensions. b Image analysis performed with a 3D optical profiler, including photographic images (left) of droplets on the smart textile surfaces and a graph (right) displaying droplet sizes to demonstrate antifouling capabilities. c SEM micrographs of the smart textile surface in the offstate (top) and on-state (bottom), highlighting antifouling effects. The off-state images show bacteria attached to the surface, whereas the on-state images depict a clean surface. d Analysis of bacterial attachment under different conditions (droplet,

suspension) on smart textiles in both off/on states. **e** Measurement of weight variations in smart textiles over time in off and on states. **f** Amount of bacteria adhered to the surface of a single-pixel transducer (square-shaped PZT), including SEM micrographs of the device's surface in off and on states. **g** Comparison of the number of bacteria attached to the surface of a one-pixel transducer (circle-shaped PZT) versus a square-shaped PZT, with both demonstrating significant antifouling performance. **h** Quantification of bacteria attached to the surface of smart textiles in off/ on states after exposure to a bacterial suspension, compared with nylon textiles.

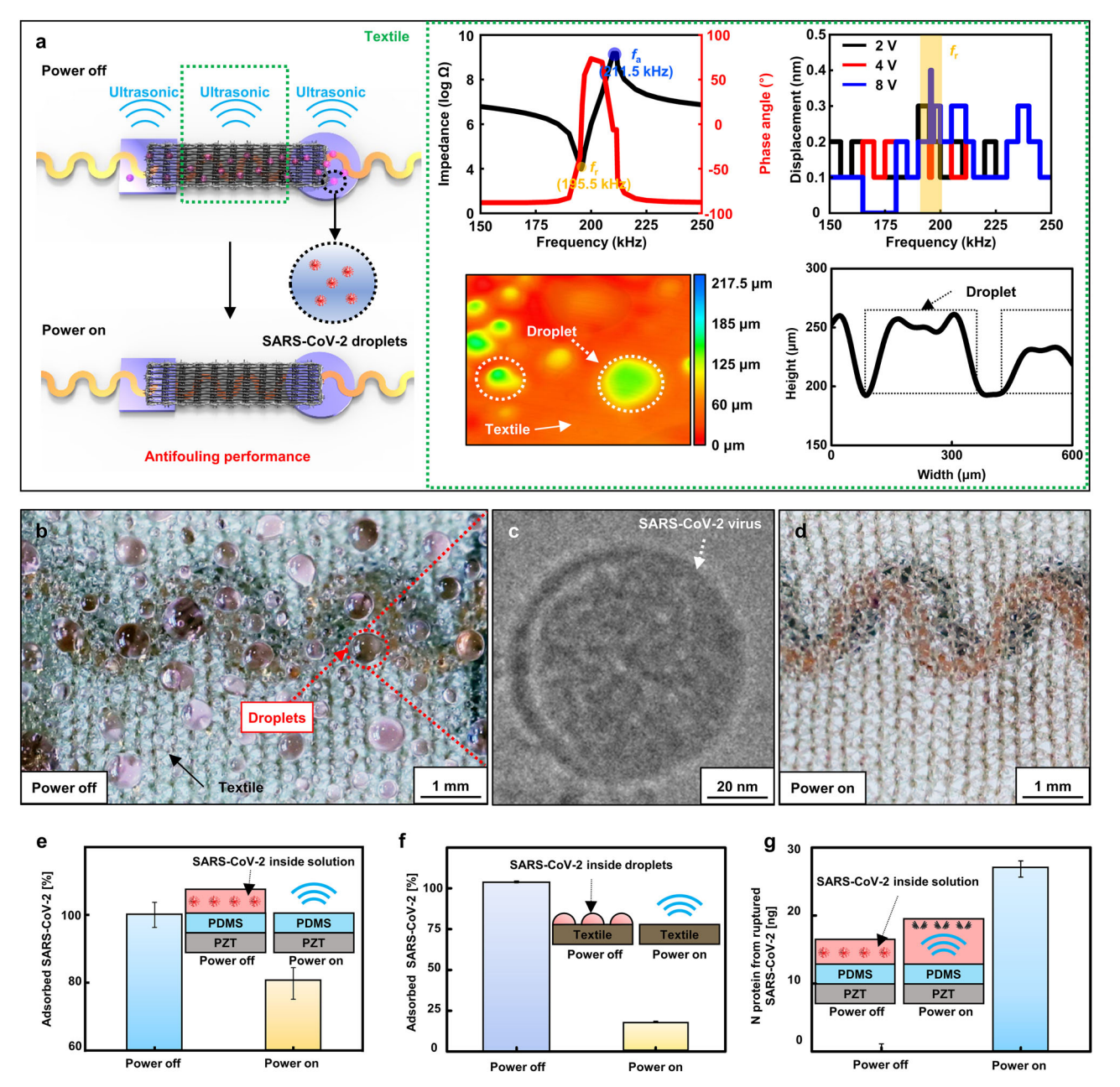


Fig. 4 | Experimental results of virus tests for antifouling and rupture performance in suspension and droplet forms. a Schematic illustrating the antifouling performance against SARS-CoV-2 droplets, and the electrical and mechanical properties of the smart textile. b Photographic image of the smart textile with

droplets in the power-off state. c Cryo-TEM image of SARS-CoV-2. d Photographic image of the textile in the power-on state. e Proportion of SARS-CoV-2 adsorbed from the suspension on the textile. f Proportion of SARS-CoV-2 adsorbed from droplets on the textile. g Measurement of N protein from disrupted SARS-CoV-2.

antifouling performance when a SARS-CoV-2 suspension is sprayed onto the smart textile. The adsorption of SARS-CoV-2 on the textile is prevented by displacements generated by the smart textile. The left graph in the inset displays the impedance and phase angle of the smart textile, with resonance frequency (f_r) at 195.5 kHz, antiresonance frequency (f_a) at 211.5 kHz, impedances (black curves), and phase angles (red curves). The textile generates a displacement of maximum \approx 0.3 nm at 2 V, \approx 0.2 nm at 4 V, and \approx 0.4 nm at 8 V, at f_r (right graph). The 3D profiler image details the droplet properties, and the graph indicates droplet sizes (diameter \leq 250 µm). Figure 4b presents a photographic image of the smart textile sprayed with a SARS-CoV-2 suspension when the device is switched off, exhibiting a large number of droplets on the surface, which includes the stretchable ultrasonic transducers and the nylon textile. Figure 4c displays representative cryogenic transmission electron microscopy (Cryo-TEM) images of the SARS-

CoV-2 used in this study. In contrast, significantly fewer droplets are observed on the surface when sprayed during the operation of the smart textile (Fig. 4d; see details of the virus experiment in the Method section).

To quantify the antifouling performance of the smart textile against SARS-CoV-2, we measure the amount of virus adsorbed. Initially, the smart textile is immersed in a highly concentrated viral suspension $(1.07\times10^{11}~{\rm copies/mL})$, where substantial adsorption was expected. Figure 4e shows that approximately 20% less SARS-CoV-2 is adsorbed by the vibrating smart textile during a 1 h incubation. This result implies that our smart textile can effectively reduce the adsorption of SARS-CoV-2 in extreme environments. To evaluate the antifouling performance in a realistic environment, we conduct the same experiment with sprayed viral droplets, as shown in Fig. 4f. Notably, the ultrasonic waves emitted by the smart textile reduced the adsorption of SARS-CoV-2 by more than 75%.

Finally, we examine whether our device could rupture the viruses. Given that ultrasonic waves can disrupt a lipid membrane ³⁹, we fabricate an optimized ultrasonic transducer with a large displacement (3.4 nm, circular-shaped ultrasonic transducer) that can rupture the viruses at the surface. After immersing the smart textile in the viral suspension and operating for 1 h, 26.8 ng of N protein was detected in the suspension, indicating virus rupture (Fig. 4g). This result shows that our smart textiles can not only reduce adsorption but also effectively rupture the viruses.

Discussion

In this study, we demonstrate the efficacy of active-type smart textiles, which are integrated with flexible devices, designed to prevent bacterial contamination and COVID-19 infections 40-43. We outline the designs, materials, and operating principles of piezoelectric smart textiles. These active-type wearable platforms, which incorporate ultrasonic transducers 44,45, stretchable interconnector arrays 6, and polymeric fabric, exhibited antifouling performance against bacteria (*E. coli*) and viruses (SARS-CoV-2). They also maintained stable performance under harsh conditions, such as in the presence of bacterial droplets and high concentrations of viral suspensions. Moreover, the piezoelectric transducers demonstrated rupturing performance against SARS-CoV-2.

The performance of the smart textiles was confirmed through experimental results, including an analysis of optical images, an examination of the properties of bacteria and viruses attached to the surface of the textiles, and a quantitative analysis of N proteins generated from the ruptured viruses. We anticipate that these significant results will provide an effective method to reduce the spread of COVID-19. These textiles are a crucial strategy for medical staff exposed to high concentrations of bacteria and viruses, offering substantial potential as a preventive measure during outbreaks of infectious variants. The integration of sensing devices, along with the introduction of self-power generation and wireless systems, will enable PZT-based ultrasound wearable devices to be adapted to various form factors.

Methods

Fabrication of smart textiles

The fabrication of smart textiles encompasses three primary stages: (i) the fabrication of stretchable electrodes; (ii) the assembly of the ultrasonic device; and (iii) the integration of the elements. (i) In the first stage, a 3 µmthick PI layer (poly(pyromellitic dianhydride-co-4,4'-oxydianiline) amic acid solution, Sigma-Aldrich, Republic of Korea) is coated on a 20 µm-thick Cu film, to create flexible electrodes 47,48. This is achieved by spin-coating the PI on the Cu film at 3000 rpm for 30 s, followed by a sequential baking process on a hotplate at temperatures of 110 °C, 160 °C, and 180 °C for 10 min each, and culminating with a full cure in a vacuum oven at 180 °C for 1 h. The PI/Cu films are patterned into curved lines using pulsed laser ablation, as depicted in Fig. 1a (designed by Auto CAD software). The laser parameters include a central wavelength of 1059-1065 nm, power of 0.228 mJ, frequency of 35 kHz, speed of 300 mm/s, and pulse width of 500 ns, which are specifically employed for patterning the Cu electrodes⁴⁹. (ii) In the second stage, flexible circuits are soldered to ultrasonic transducers using Ag paste (P-100, El-Coat, Republic of Korea) for the top and bottom electrodes. (iii) In the final stage, these transducers are affixed to pre-cut PDMS substrates (10:1, Sylgard 184, Dow Corning, USA) matching the shapes of the PZT. The PDMS substrate is prepared by spin-coating at 1000 rpm for 60 s and cured at room temperature for 12 h. The devices are subsequently encapsulated with PDMS (10:1) and integrated with nylon fabric (refer to Supplementary Fig. 7 and Supplementary Fig. 8) before curing at room temperature for an additional 12 h.

Characterization of PZT

A homogeneous rhombohedral perovskite structure (JCPDS #86-1712) is confirmed in all PZT specimens, as detailed in Supplementary Fig. 9. The lattice parameters and inter-axial angle for all specimens are consistently $a=b=c=4.045~\mbox{Å}$ and $\alpha=89.8^{\circ}$, respectively. The ferroelectric hysteresis

(P-E) curve was obtained at a fixed frequency of 1 Hz using a ferroelectric measurement system (TF analyzer 1000, aixACCT Systems GmbH, Germany). Measurements were conducted in silicon. Additionally, the dielectric properties, including the dielectric constant ($\epsilon_{33}^{\rm T}/\epsilon_0$) and dielectric loss (tan δ), were measured using an impedance analyzer (Agilent Technologies HP 4294 A, Santa Clara, USA). The $\epsilon_{33}^{\rm T}/\epsilon_0$ and tan δ values for PZT-PZNN are 3360 and 0.042, respectively.

Poling of PZT and electrical testing of PZT

Calcined commercial PZT powder (MPT, Hayashi Chemical, Japan) was pressed into discs at a pressure of 100 kgf/cm² and sintered at 1050 °C for 4 h. Subsequently, silver (Ag) paste was screen-printed onto the sintered specimens and fired at 550 °C for 10 min. The PZT ceramics were poled in silicone oil by applying a DC field of 4 kV/mm for 30 min at 100 °C. The active electrode areas of the square-shaped and circle-shaped PZT transducers are 0.25 cm² and 1.13 cm², respectively. The poling field and temperature conditions were set, with PZT-PZNN and commercial PZT (MPT) exhibiting coercive electric fields of ≈0.8 kV and ≈1 kV, respectively, as illustrated in Fig. 1d and Supplementary Fig. 10. The poling field was intentionally set higher than the coercive electric field to ensure complete alignment of the polarization in the desired direction. Furthermore, temperature influences the mobility of charged defects, domain wall movement, and the kinetics of polarization reversal, necessitating an optimal temperature range for poling. Given that the Curie temperature of PZT materials, where the material transitions from ferroelectric to paraelectric states, ranges from 200 to 400 °C, poling temperatures typically vary from 60 to 120 °C. The structural properties of the PZT ceramics were characterized using XRD (D/max-RC, Rigaku, Japan) and SEM (S-4300, Hitachi, Japan). Additionally, the ferroelectric hysteresis (P-E) curve was obtained using a ferroelectric measurement system (TF analyzer 1000, aixACCT Systems GmbH, Germany).

Measurement of hysteresis of PZT

Conventional ferroelectric hysteresis (P-E) measurements were utilized to plot the hysteresis curve. After the application of the preset pulse, a remanent polarization (+P_r) of $\approx\!20~\mu\text{C/cm}^2$ was observed. With the application of the triangular bipolar field pulse, polarization reached saturation at the maximum electric field and diminished to zero upon reaching the coercive electric field (+E_c). As the electric field was reduced to zero, a remanent polarization (-P_r) remained. Thereafter, polarization again reached saturation at the negative maximum electric field and increased to zero as the negative coercive electric field (-E_c) was attained. Finally, as the electric field was restored to zero, the polarization incrementally increased.

Electromechanical and mechanical analysis of the ultrasonic transducers

An impedance analyzer (Agilent Technologies) was employed to measure the impedance and phase angle of the ultrasonic transducer across a frequency range of 40 Hz to 110 MHz. The resonant frequency ($f_{\rm a}$) of the ultrasonic transducers, both square and circular, were also measured. Additionally, the displacement of the ultrasonic transducer, which was equipped with a laser reflection tape (dimensions = 5 mm × 5 mm, thickness \approx 1 mm), was quantified using a laser number measuring instrument.

FEA simulations

The mechanical response of Nylon textile and Cu electrodes was evaluated using biaxial tensile tests conducted through finite element (FE) simulations with ABAQUS/Explicit (Dynamic, Explicit procedure). Material properties such as Young's modulus (E) and Poisson's ratio (ν) for both textile and Cu electrodes were derived from previous studies ^{50–52}, with E_{Nylon} of 2700 MPa, E_{Cu} of 119,000 MPa, ν_{Nylon} of 0.39, and ν_{Cu} of 0.34. Additionally, yield strength values for the electrodes, obtained from previously published experimental data, were incorporated into the simulations. Proper boundary conditions were implemented during the tensile test (see details in

Supplementary Note 2): the bottom and left parts of the electrodes were constrained in both direction and position, specified by the displacement settings (bottom of U1 = U3 = UR1 = UR2 = UR3 = 0 and left of U2 = U3 = UR1 = UR2 = UR3 = 0). The interface between the textile and electrodes was secured using the *Tie* constraint of the *Interaction Module*. The structural configuration employed hybrid hexahedral elements (C3D8H) for the nylon layer and reduced integration hexahedral elements (C3D8R) for the electrode layer. The electrode's element size was set at 0.15 mm, resulting in a mesh comprising 14,983 electrodes. The biaxial tensile test adjusted the boundary conditions to elongate the model by 30% in both axial directions.

Grid independence test

A grid independence study was conducted by evaluating the maximal principal strain across six different grids with element numbers of 547, 1462, 5433, 14,983, 20,488, and 41,596. The results from these grids were compared to determine the optimal balance between computational efficiency and accuracy (refer to Supplementary Fig. 11 for details). The analysis revealed negligible differences in the results when comparing the smaller grids to the grid with 14,983 elements. Consequently, to optimize computational time while maintaining accuracy, the grid consisting of 14,983 elements was selected for subsequent computations⁵³.

Bacterial cultures

The working cultures of *Escherichia coli* (ATCC 25922; Korean Culture Center of Microorganisms, Seoul, Republic of Korea) were prepared by transferring a portion of the culture from tryptic soy agar (TSA; Becton, Dickinson and Co., Franklin Lakes, NJ, USA) using a loop to 9 mL of tryptic soy broth (TSB; same manufacturer). This mixture was incubated at 37 °C for 24 h. Subsequent to this initial incubation, the culture was transferred to fresh TSB using a 20 μL loop and incubated again at 37 °C for an additional 24 h. The final concentrations of the cultured *E. coli* ranged from 8.5 to 9.0 log CFU/mL.

Dip-inoculation

The inoculation process involves immersing the ultrasonic transducer and smart textile in 5 mL of a bacterial suspension, with concentrations ranging from 8.6 to 9.0 log CFU/mL, at room temperature. This step is performed for 1 h while the devices are in a power-on state.

Bacterial adhesion assay

The inoculation process entails immersing smart textiles in 5 mL of a bacterial suspension, with concentrations ranging from 8.5 to 9.0 log CFU/mL, at room temperature for 1 h, while the devices are powered on. The assessment of bacterial adhesion on each sample surface was performed using the pour plate method. This method involves enumerating viable bacteria by counting the total number of colony-forming units (CFU). After inoculation, the devices were transferred into 9 mL of 0.1% (w/v) peptone water and vortexed for 1 min to detach bacteria from their surfaces. Subsequent serial dilutions were performed, and 1 mL of peptone water containing bacteria was plated onto tryptic soy agar (TSA). The bacteria were incubated for 24 h at 37 °C under aerobic conditions. The resulting bacterial densities indicated the quantity of bacteria attached to the surfaces. Additionally, the analysis of bacteria attached to the devices was conducted using SEM. Devices that had been immersed in the bacterial suspension for one hour were prepared for SEM imaging by depositing a thin layer of platinum (14 nm) on their surfaces to ensure adequate electrical conductivity.

SARS-CoV-2 specimen collection

Inactivated SARS-CoV-2 was provided by the Korea Center for Disease Control and Prevention. Throat swabs from COVID-19 patients were used to extract SARS-CoV-2. The Vero E6 cell line was utilized to subculture the collected SARS-CoV-2 across two passages. The virus was inactivated *via* thermal treatment, involving the following procedure: Two 175 T flasks containing 1×10^7 Vero E6 cells each were prepared. Each flask was

inoculated with 100 μ L of live virus (6.5 × 10⁶ PFU/mL) in a medium containing 2% fetal bovine serum (FBS) and 1% penicillin (PS). After three days, following the observation of a cytopathic effect, the virus was harvested. The harvested suspension was centrifuged to remove cells, and the supernatant was transferred to a 50 mL tube. To inactivate the virus, this tube was subjected to a thermal treatment in a 70 °C water bath for 1 h (P0). Subsequently, Vero E6 cells were seeded in a 12-well plate (2 × 10⁵ cells/well) and inoculated with the virus suspension. The cytopathic effect (CPE) was monitored over five days (P1). After confirming the absence of observed CPE, the inoculation was repeated (P2). Finally, ribonucleic acids were extracted from the P0–P3 suspensions, and the Ct values of the R/E gene were measured to verify any changes in virus quantity. The Ct values obtained were P0: 13.36/12.15, P1: 22.1/19.83, and P2: 27.73/25.1, indicating a decrease in viral RNA. The concentration of the virus suspension used in the study was 1.07×10^{11} copies/mL.

Adsorption and rupture experiments of SARS-CoV-2

The adsorption of SARS-CoV-2 on smart textiles and transducers was monitored by measuring the N protein levels. The devices were exposed to the virus either by droplet application or by full immersion in the virus suspension. Following 1 h of exposure, the surfaces were thoroughly washed with PBS at least thrice. Subsequently, the devices were immersed in a virus lysis suspension [comprising 50 mM Tris(hydroxymethyl)aminomethane (TRIS) and 0.05% sodium azide] for 30 min to release the N protein from the adsorbed SARS-CoV-2. The concentration of N protein in the lysate was quantified using an enzyme-linked immunosorbent assay kit (Abcam, USA). The resulting standard curve demonstrated an R² value of 0.998, as detailed in Supplementary Fig. 12. Additionally, to disrupt SARS-CoV-2, an ultrasonic transducer equipped with a larger displacement membrane (3.4 nm) was employed. The transducer was immersed in the virus suspension and operated at its resonant frequency (f_r) for 1 h. After this incubation period, the suspension was collected, and the amount of released N protein was measured to assess the efficacy of the transducer in disrupting the viral membrane.

Reusability test of ultrasonic transducer

Reusability tests on smart textiles composed of unit pixels of square and circular ultrasonic transducers. One cycle was performed by soaking the smart textile in DI water for 5 minutes and then drying it at room temperature for 5 minutes. Electrical properties were examined after each cycle was repeated up to 100 times (Supplementary Fig. 13).

Data availability

The data that support the findings of this study are either provided in the source data or are available from the corresponding author upon reasonable request.

Received: 4 February 2024; Accepted: 26 September 2024; Published online: 09 October 2024

References

- Ferretti, L. A.-O. et al. Quantifying SARS-CoV-2 transmission suggests epidemic control with digital contact tracing. Science 368, eabb6936 (2020).
- Guan, W.-J. et al. Clinical characteristics of coronavirus disease 2019 in China. N. Engl. J. Med. 382, 1708–1720 (2020).
- Hongdou, L. et al. Age-dependent risks of Incidence and mortality of COVID-19 in Hubei province and other parts of China. medRxiv 7, 190 (2020).
- Yang, L. et al. COVID-19: immunopathogenesis and Immunotherapeutics. Signal Transduct. Target. Ther. 5, 128 (2020).
- Jeyanathan, M. et al. Immunological considerations for COVID-19 vaccine strategies. Nat. Rev. Immunol. 20, 615–632 (2020).
- Malik, A. A., McFadden, S. M., Elharake, J. & Omer, S. B. Determinants of COVID-19 vaccine acceptance in the US. eClinicalMedicine 26, 100495 (2020).

- McKay, P. F. et al. Self-amplifying RNA SARS-CoV-2 lipid nanoparticle vaccine candidate induces high neutralizing antibody titers in mice. Nat. Commun. 11, 3523 (2020).
- Laczkó, D. et al. A single immunization with nucleoside-modified mRNA vaccines elicits strong cellular and humoral immune responses against SARS-CoV-2 in mice. *Immunity* 53, 724–732.e7 (2020).
- Tahir ul Qamar, M. et al. Epitope-based peptide vaccine design and target site depiction against middle east respiratory syndrome coronavirus: an immune-informatics study. *J. Transl. Med.* 17, 362 (2019).
- Ali, M. A. et al. Sensing of COVID-19 antibodies in seconds via aerosol jet nanoprinted reduced-graphene-oxide-coated 3D electrodes. Adv. Mater. 33, 2006647 (2021).
- Haniff, H. S. et al. Targeting the SARS-CoV-2 RNA genome with small molecule binders and ribonuclease targeting chimera (RIBOTAC) degraders. ACS Cent. Sci. 6, 1713–1721 (2020).
- Hirschmann, M. T. et al. COVID-19 coronavirus: recommended personal protective equipment for the orthopaedic and trauma surgeon. *Knee Surg. Sports Traumatol. Arthrosc.* 28, 1690–1698 (2020).
- Holland, M., Zaloga, D. J. & Friderici, C. S. COVID-19 Personal Protective Equipment (PPE) for the emergency physician. Vis. J. Emerg. Med. 19, 100740 (2020).
- Ates, H. C., Yetisen, A. K., Güder, F. & Dincer, C. Wearable devices for the detection of COVID-19. Nat. Electron. 4, 13–14 (2021).
- Yetisen, A. K., Martinez-Hurtado, J. L., Ünal, B., Khademhosseini, A. & Butt, H. Wearables in medicine. Adv. Mater. 30, 1706910 (2018).
- Morales-Narváez, E. & Dincer, C. The impact of biosensing in a pandemic outbreak: COVID-19. *Biosens. Bioelectron.* 163, 112274 (2020).
- Cheong, S. H. R., Ng, Y. J. X., Lau, Y. & Lau, S. T. Wearable technology for early detection of COVID-19: a systematic scoping review. *Prev. Med.* 162, 107170 (2022).
- Li, Y., Huang, X, Yu, I T S, Wong, T W Wong & Qian, H. Role of air distribution in SARS transmission during the largest nosocomial outbreak in Hong Kong. *Indoor Air* 15, 83–95 (2005).
- Otter, J. A. et al. Transmission of SARS and MERS coronaviruses and influenza virus in healthcare settings: the possible role of dry surface contamination. J. Hosp. Infect. 92, 235–250 (2016).
- Ong, S. W. X. et al. Air, surface environmental, and personal protective equipment contamination by severe acute respiratory syndrome coronavirus 2 (SARS-CoV-2) from a symptomatic patient. *JAMA* 323, 1610–1612 (2020).
- Bai, Y. et al. Presumed asymptomatic carrier transmission of COVID-19. JAMA 323, 1406–1407 (2020).
- Bi, Q. et al. Epidemiology and transmission of COVID-19 in 391 cases and 1286 of their close contacts in Shenzhen, China: a retrospective cohort study. *Lancet Infect. Dis.* 20, 911–919 (2020).
- Ali, M. A. et al. N protein-based ultrasensitive SARS-CoV-2 antibody detection in seconds via 3D nanoprinted, microarchitected array electrodes. J. Med. Virol. 94, 2067–2078 (2022).
- Ali, M. A. et al. Breaking the barrier to biomolecule limit-of-detection via 3D printed multi-length-scale graphene-coated electrodes. *Nat. Commun.* 12, 7077 (2021).
- Ni, X. et al. Automated, multiparametric monitoring of respiratory biomarkers and vital signs in clinical and home settings for COVID-19 patients. *Proc. Natl. Acad. Sci.* 118, e2026610118 (2021).
- Jasmine, A. & Jayanthy, A. K. Sensor-based system for automatic cough detection and classification. *Test Eng. Manag.* 83, 13826–13834 (2020).
- Amrulloh, Y. A., Abeyratne, U. R., Swarnkar, V., Triasih, R. & Setyati, A. Automatic cough segmentation from non-contact sound recordings in pediatric wards. *Biomed. Signal Process. Control.* 21, 126–136 (2015).

- Zhong, H. et al. Reusable and recyclable graphene masks with outstanding superhydrophobic and photothermal performances. ACS Nano 14. 6213–6221 (2020).
- El-Atab, N., Qaiser, N., Badghaish, H., Shaikh, S. F. & Hussain, M. M. Flexible nanoporous template for the design and development of reusable anti-COVID-19 hydrophobic face masks. ACS Nano 14, 7659–7665 (2020).
- Avelelas, F. et al. Efficacy and ecotoxicity of novel anti-fouling nanomaterials in target and non-target marine species. *Mar. Biotechnol.* 19, 164–174 (2017).
- Mahmoudpour, M., Jouyban, A., Soleymani, J. & Rahimi, M. Rational design of smart nano-platforms based on antifouling-nanomaterials toward multifunctional bioanalysis. *Adv. Colloid Interface Sci.* 302, 102637 (2022).
- Mauter, M. S. et al. Antifouling ultrafiltration membranes via postfabrication grafting of biocidal nanomaterials. ACS Appl. Mater. Interfaces 3, 2861–2868 (2011).
- Ong, C. S., Goh, P. S., Lau, W. J., Misdan, N. & Ismail, A. F. Nanomaterials for biofouling and scaling mitigation of thin film composite membrane: a review. *Desalination* 393, 2–15 (2016).
- Seo, I. et al. Fabrication and characterization of low temperature sintered hard piezoelectric ceramics for multilayer piezoelectric energy harvesters. Ceram. Int. 47, 16688–16695 (2021).
- Hu, H. et al. Stretchable ultrasonic transducer arrays for threedimensional imaging on complex surfaces. Sci. Adv. 4, eaar3979 (2018).
- Kim, B. H. et al. Three-dimensional silicon electronic systems fabricated by compressive buckling process. ACS Nano 12, 4164–4171 (2018).
- 37. Arumugam, V., Naresh, M. D. & Sanjeevi, R. Effect of strain rate on the fracture behaviour of skin. *J. Biosci.* **19**, 307–313 (1994).
- Wang, C. et al. Monitoring of the central blood pressure waveform via a conformal ultrasonic device. Nat. Biomed. Eng. 2, 687–695 (2018).
- 39. Kang, M., Huang, G. & Leal, C. Role of lipid polymorphism in acoustically sensitive liposomes. *Soft Matter* **10**, 8846–8854 (2014).
- Oh, N. et al. Double-heterojunction nanorod light-responsive LEDs for display applications. Science 355, 616–619 (2017).
- Kim, B. H. et al. High-resolution patterns of quantum dots formed by electrohydrodynamic jet printing for light-emitting Diodes. *Nano Lett* 15, 969–973 (2015).
- Pang, W. et al. A soft microrobot with highly deformable 3D actuators for climbing and transitioning complex surfaces. *Proc. Natl. Acad. Sci.* 119, e2215028119 (2022).
- Zhao, H. et al. Mechanically guided hierarchical assembly of 3D mesostructures. Adv. Mater. 34, 2109416 (2022).
- 44. Park, K.-I. et al. Piezoelectric BaTiO3 thin film nanogenerator on plastic substrates. *Nano Lett* **10**, 4939–4943 (2010).
- Park, K. I. et al. Highly-efficient, flexible piezoelectric PZT thin film nanogenerator on plastic substrates. *Adv. Mater.* 26, 2514–2520 (2014).
- Liu, Y. et al. Electronic skin as wireless human-machine interfaces for robotic VR. Sci. Adv. 8, eabl6700 (2022).
- 47. Choi, S.-H. et al. Selective acetate detection using functional carbon nanotube fiber. *J. Sens. Sci. Technol.* **30**, 357–363 (2021).
- Suh, J. M. et al. Synthesis of nanoporous metal oxide films using anodic oxidation and their gas sensing properties. *J. Sens. Sci. Technol.* 27, 13–20 (2018).
- Shim, Y.-S. et al. Design of metal oxide hollow structures using softtemplating method for high-performance gas sensors. *J. Sens. Sci. Technol.* 25, 178–183 (2016).
- Won, S. M. et al. Multimodal sensing with a three-dimensional piezoresistive structure. ACS Nano 13, 10972–10979 (2019).
- Chung, H. U. et al. Binodal, wireless epidermal electronic systems with in-sensor analytics for neonatal intensive care. Science 363, eaau0780 (2019).

- 52. Kim, B. H. et al. Mechanically guided post-assembly of 3D electronic systems. *Adv. Funct. Mater.* **28**, 1803149 (2018).
- Hu, H. et al. CFD analysis of the aerodynamic characteristics of biconvex airfoil at compressible and high Mach numbers flow. SN Appl. Sci. 1, 1283 (2019).

Acknowledgements

This work was supported by the National Research Foundation of Korea (NRF) Grant funded by the Korea government (MSIT) (No. RS-2024-00347619, No. RS-2024-00407155, 2022M3H4A1A02046445, RS-2023-00209955, and RS-2024-00406240). This research was supported by the Nano & Material Technology Development Program through the National Research Foundation of Korea (NRF) funded by Ministry of Science and ICT (RS-2024-00452380). This work was supported by Korea Institute of Planning and Evaluation for Technology in Food, Agriculture and Forestry (IPET) through High-Risk Animal infectious Disease Control Technology Development Program, funded by Ministry of Agriculture, Food and Rural Affairs (MAFRA)(RS-2024-00396818). We confirm that we created all the elements used in the figures, including Fig. 1, and do not contain any third-party content.

Author contributions

S.E.L., H.L., J.H.K., and J.C.P. contributed equally to this work. B.H.K. conceived the idea and supervised the overall work. S.E.L., H.L., J.H.K., J.C.P., S.H.H., J.K.O., and B.H.K. conceived of the overall research goals and aims. S.E.L., J.H.K., J.H.P., S.H.H., and B.H.K. fabricated the devices and PZT-based transducers. H.L., H.C., S.H.B., and J.K.O. performed bacterial tests, data collection, and analysis. J.C.P., J.-M.K., H.-J.J., and H.K. performed viral tests, data collection, and analysis. S.K., S.P., and J.K. performed mechanical simulations and characterizations. S.E.L., J.H.P., J.H.K., S.H.C., S.H.H., and B.H.K. performed characterizations of transducers. S.E.L., H.L., J.H.K., J.C.P., S.H.H., J.K.O., and B.H.K. wrote the manuscript. All authors discussed the results and commented on the manuscript.

Competing interests

The authors declare no competing interests.

Additional information

Supplementary information The online version contains supplementary material available at https://doi.org/10.1038/s41528-024-00350-y.

Correspondence and requests for materials should be addressed to Seung Ho Han, Jun Kyun Oh or Bong Hoon Kim.

Reprints and permissions information is available at http://www.nature.com/reprints

Publisher's note Springer Nature remains neutral with regard to jurisdictional claims in published maps and institutional affiliations.

Open Access This article is licensed under a Creative Commons Attribution 4.0 International License, which permits use, sharing, adaptation, distribution and reproduction in any medium or format, as long as you give appropriate credit to the original author(s) and the source, provide a link to the Creative Commons licence, and indicate if changes were made. The images or other third party material in this article are included in the article's Creative Commons licence, unless indicated otherwise in a credit line to the material. If material is not included in the article's Creative Commons licence and your intended use is not permitted by statutory regulation or exceeds the permitted use, you will need to obtain permission directly from the copyright holder. To view a copy of this licence, visit http://creativecommons.org/licenses/by/4.0/.

© The Author(s) 2024